Measurement of Body-Centered-Cubic Aluminum at 475 GPa

D. N. Polsin, D. E. Fratanduono, J. R. Rygg, A. Lazicki, R. F. Smith, J. H. Eggert, M. C. Gregor, B. H. Henderson, J. A. Delettrez, R. G. Kraus, P. M. Celliers, F. Coppari, D. C. Swift, C. A. McCoy, C. T. Seagle, J.-P. Davis, S. J. Burns, G. W. Collins, and T. R. Boehly

Measurement of body-centered-cubic aluminum at 475 GPa

D. N. Polsin,[1, 2, ∗] D. E. Fratanduono,[3] J. R. Rygg,[1, 2, 4] A. Lazicki,[3] R. F. Smith,[3] J. H. Eggert,[3] M. C. Gregor,[3] B. H. Henderson,[1, 2] J. A. Delettrez,[1] R. G. Kraus,[3] P. M. Celliers,[3] F. Coppari,[3] D. C. Swift,[3] C. A. McCoy,[5] C. T. Seagle,[5] J.-P. Davis,[5] S. J. Burns,[4] G. W. Collins,[1, 2, 4] and T. R. Boehly[1]

[1]*Laboratory for Laser Energetics, University of Rochester, Rochester, New York 14623-1299, USA*
[2]*Department of Physics and Astronomy, University of Rochester, Rochester, New York 14627, USA*
[3]*Lawrence Livermore National Laboratory, Livermore, California 94550, USA*
[4]*Department of Mechanical Engineering, University of Rochester, Rochester, New York 14627, USA*
[5]*Sandia National Laboratories, PO Box 5800, Albuquerque, New Mexico 87185-1189, USA*
(Dated: October 2, 2017)

Nanosecond *in-situ* x-ray diffraction and simultaneous velocimetry measurements were used to determine the crystal structure and pressure, respectively, of ramp-compressed aluminum at stress states between 111 and 475 GPa. The solid–solid Al phase transformations, fcc–hcp and hcp–bcc, are observed at 216±9 GPa and 321±12 GPa, respectively, with the bcc phase persisting to 475 GPa. The high-pressure crystallographic texture of the hcp and bcc phases suggests close-packed or nearly close-packed lattice planes remain parallel through both transformations.

PACS numbers: 62.50.-p, 61.05.cp, 64.70.K, 81.05.Bx

At standard conditions, aluminum is an *sp*-bonded metal with no *d*-band electrons, and the atoms are arranged in a face-centered cubic (fcc) crystal structure. Because of this simplicity, Al is a prototype metal for testing theoretical methods[1–4]. While Al is one of the most extensively studied materials in high-pressure shock-wave experiments [5–9], shock-compression heating and subsequent melting at shock-pressures above 125 GPa prevent such data from constraining solid-state structural calculations or from providing model-independent constraints on the low temperature equation-of-state (EOS) at extreme pressures. Diamond-anvil cell (DAC) measurements on Al have revealed an fcc–hcp transition at 217 GPa and 297 K with the hcp phase stable to 333 GPa [10]. While structural predictions for Al exist up to many terapascals [11], there are no experimental data at pressures beyond 333 GPa.

To extend such measurements to higher pressures, we developed the capability to perform *in-situ* x-ray diffraction (XRD) on ramp compressed solids [12–14]. This experimental technique allows us, in principle, to probe the structure of solids into the multi-terapascal regime. We present measurements of Al compressed to 475 GPa that reveal a high-pressure bcc phase. We report the observation of an hcp to bcc transition at 321±12 GPa, with the bcc phase persisting to at least 475 GPa. These data provide key experimental benchmarks for density functional theory calculations, which predict a sequence of phase transitions to increasingly complex structures in Al up to tens of terapascals [11]. In addition, our experiments show that both the fcc–hcp and hcp–bcc solid–solid phase transitions occur at nanosecond compression time scales. The observed material texture evolution through the transitions provides insight into the atomic pathways.
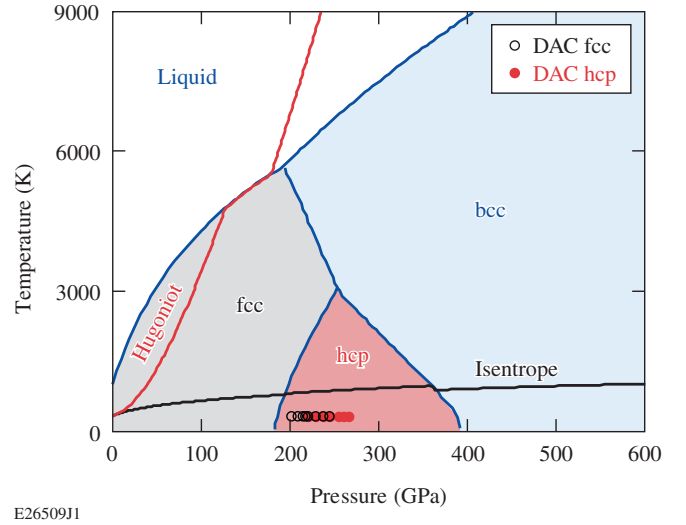
A theoretical phase diagram calculated using DFT

FIG. 1: Theoretical phase diagram of Al from Ref. [15] calculated using DFT methods. DAC data from Ref. [10] are shown for the fcc and hcp phases.

methods for the solid and liquid phases of Al at extreme pressures and temperatures [15] is shown in Fig. 1. Phonon spectra calculations were performed by Ref. [15] to include thermal effects. Along the principal Hugoniot, fcc Al melts at 125 to 150 GPa [16, 17] while the Al principal isentrope exhibits two solid–solid phase transitions, one from fcc to hcp at 195 GPa (780 K) and another to bcc at 363 GPa (920 K), as calculated by [15]. The fcc-hcp-bcc triple point is calculated at 255 GPa and 2900 K. The static XRD data at 297 K are shown for the fcc and hcp phases [10]. A superdense bcc allotrope of Al has been synthesized and recovered at ambient conditions [18].

To explore the high-pressure Al solid-state structure

up to and above the predicted hcp–bcc transition pressure, ramp-compression experiments were performed on the OMEGA EP laser [19]. Temporally shaped 351-nm laser pulses smoothly increased the applied pressure over 10 ns on Al targets. A single beam with a 1100-μm focal spot drove targets with 10-ns pulses and laser intensity that ramped up to 3.4 $\times10^{13}$ W/cm^2. An additional beam irradiated a separate Cu or Ge backlighter target to produce 8.37-keV or 10.25-keV Helium-like emission (He$_\alpha$) x rays that probed the compressed Al for 1 ns. The Al (99.999% purity) samples were rolled foils obtained from Goodfellow Inc. or electron-beam–deposited 15-μm coatings on LiF. The rolling resulted in the strong preferred orientation (texture) of the crystal grains evident in the diffraction data. The Al samples (15 or 20 μm thick) were sandwiched between a $\langle110\rangle$ oriented 20 μm single-crystal diamond ablator/pusher and a $\langle100\rangle$ oriented 100-μm or 150-μm-thick single-crystal LiF window. The Al target is mounted on either a tungsten or platinum plate with a 300-μm-diam pinhole aperture to provide x ray collimation and to restrict the field-of-view of the diagnostics to the center of the 1100-μm driven region of the target. XRD data were recorded on image plates (IPs) mounted inside the powder XRD image plate (PXRDIP) diagnostic[20]. The backlighter was mounted at 23° with respect to the Al target normal, and the x-ray emission was timed to probe the pressure plateau in the Al stress profile. The dimensions of the sandwich target stack are chosen in conjunction with a carefully designed laser pulse shape to hold the pressure in the Al constant during the x-ray exposure.

The Debye–Scherrer rings from the compressed polycrystalline samples were recorded on IP's held in the diagnostic. IP data analysis involves mapping IP pixels onto the scattering angle, 2θ, according to Ref. [20]. The Bragg condition was used to calculate the lattice d-spacings (d) of the diffracting crystals from the measured diffraction angles (2θ). The 2θ and d-spacing resolution for each peak is 1° and 2.7% [Ge x-ray source (XRS)] and 2.2% (Cu XRS), respectively, considering spectral broadening, finite XRS size, and finite pinhole diameter.

Velocimetry provided a measurement of *in-situ* particle velocities that were used to determine the stress state in the Al sample. A line-imaging velocity interferometer for any reflector (VISAR)[21] detects the Doppler shifts of a 532-nm probe beam reflected off the Al–LiF interface to measure *in-situ* interface velocity as a function of time. The method of characteristics was used to determine the stress distribution within the finite thickness Al sample using the interface velocity measurement as a boundary condition. The mean and standard deviation from a Monte Carlo (MC) error analysis are given as the value and uncertainty for the measured pressure during the x-ray exposure. The MC routine randomly calls either the free-energy-based *SESAME* 7271 EOS or the more-compressible *SESAME* 7271v3 EOS for LiF and

randomly uses either a power law or linear apparent to true interface velocity relation proposed by Refs. [22] and [23], respectively. Shots with large standard deviations (> 20 GPa) in the mean stress state of the sample at the time of x ray exposure were omitted. The standard deviation of the mean stress state in the sample at the time of x-ray exposure ranged from 3.2% to 6.5% of the mean pressure.
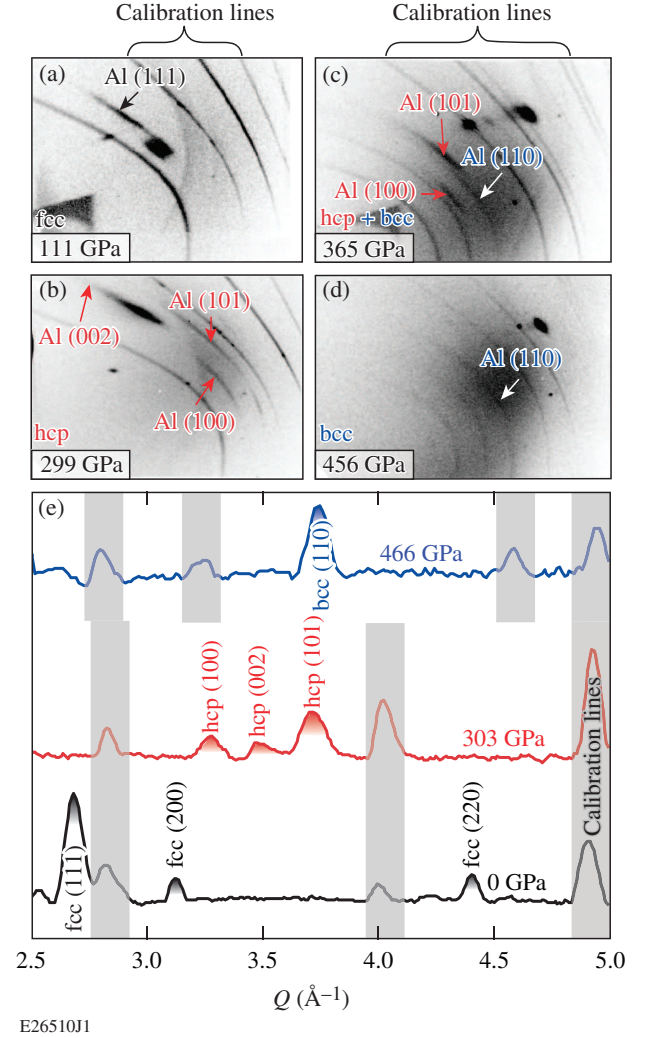

FIG. 2: OMEGA EP image plate (IP) data show (a) fcc and (b) hcp Al diffraction and ambient density W pinhole diffraction at 111 GPa and 299 GPa using a Cu x-ray source (XRS). (c) IP data at 365 GPa, with a Pt pinhole and Ge XRS show both hcp and bcc Al diffraction. (d) At 456 GPa, with a Pt pinhole and Ge XRS the hcp lines disappear and a single Al bcc (110) line is observed. (e) Lineouts (from different shots) along Q [$Q = (4\pi/\lambda)\sin(\theta)$], for an x-ray wavelength, λ, from 2θ–ϕ projections of IP data at 0 GPa ($\lambda = 1.48$ Å), 303 GPa ($\lambda = 1.48$ Å), and 466 GPa ($\lambda = 1.21$ Å) in the fcc, hcp, and bcc phases, respectively. The gray shaded regions label diffraction peaks from ambient density Pt and W used as calibration markers. The Al peaks are labeled with their structure and *hkl* plane.

Examples of XRD data are shown in Fig. 2. Diffraction lines recorded on a single PXRDIP IP from four OMEGA shots are shown in Figs. 2(a)–2(d). The data at 111 GPa in Fig. 2(a) show only the (111) line from fcc Al because of the strong initial texture of the rolled Al foil; the (200) fcc line was observed on another IP not shown here. At 299 GPa [Fig. 2(b)], the (100), (002), and (101) lines from hcp Al were observed. At 365 GPa [Fig. 2(c)], the (110) line from bcc Al was seen along with the hcp lines. The new bcc diffraction line is distinguishable from the hcp diffraction lines because it is less textured. At 456 GPa [Fig. 2(d)], the (110) bcc line persists, but the hcp lines completely disappear. The bcc phase is observed to 475 GPa, the highest pressure reached in these experiments. At 475 GPa, the observed 2θ indicates a density of 6.9 ± 0.1 g/cm^3 and a lattice parameter $a = 2.35\pm0.01$ Å. A single peak in the bcc phase is observed because the XRD diagnostic is less sensitive to high angle scattering than low angle scattering due in part to the aspect ratio of the cylindrical aperture and the small XRS incidence angle. Also, as the temperature of the Al is increased at higher pressures in the bcc phase, the Debye-Waller effect begins to decrease the intensity of the higher angle peaks due to thermal motion creating a large mean-square displacement of the atoms. Shocks were only observed in experiments above 415 GPa with a jump of 1.3 km/s in the Al–LiF interface velocity ($\smile$25 GPa, $\smile$600 K) being the strongest shock from the diamond Hugoniot elastic limit (HEL). Azimuthally averaged lineouts of the Debye–Scherrer rings from the three phases of Al are shown in Fig. 2(e) for Al at 0 GPa (undriven), 303 GPa, and 466 GPa.

Data from 24 OMEGA shots are shown in Fig. 3(a), which is a plot of the d-spacing deduced from the XRD data versus the Al stress inferred from VISAR. Individual diffraction peaks are plotted as solid points according to their phase (fcc: black; hcp: red; bcc: blue). The data are compared to the Kerley 3700 isentrope [24]. Each shot was at a unique pressure; therefore, multiple points in a vertical line indicate multiple diffraction lines observed on a single shot. The onset of the fcc–hcp transition was observed at 216±9 GPa and the hcp–bcc transition onset at 321±12 GPa. The quoted pressure for the fcc–hcp transition is the lowest measured pressure where the hcp (101) reflection was observed. The quoted pressure for the hcp–bcc transformation is the lowest measured pressure where the bcc (110) line was observed. The error in the onset pressure for these transformations is given as the experimental error in the pressure determination for the given shot.

XRD data at pressures near the transition pressures, having diffraction lines from multiple phases, suggest the coexistence of states. Despite the finite Al sample thickness and the 1-ns probe duration, the inferred pressure distributions in the Al are not large enough to explain the coexistence observed over a 22 GPa and 43 GPa range,
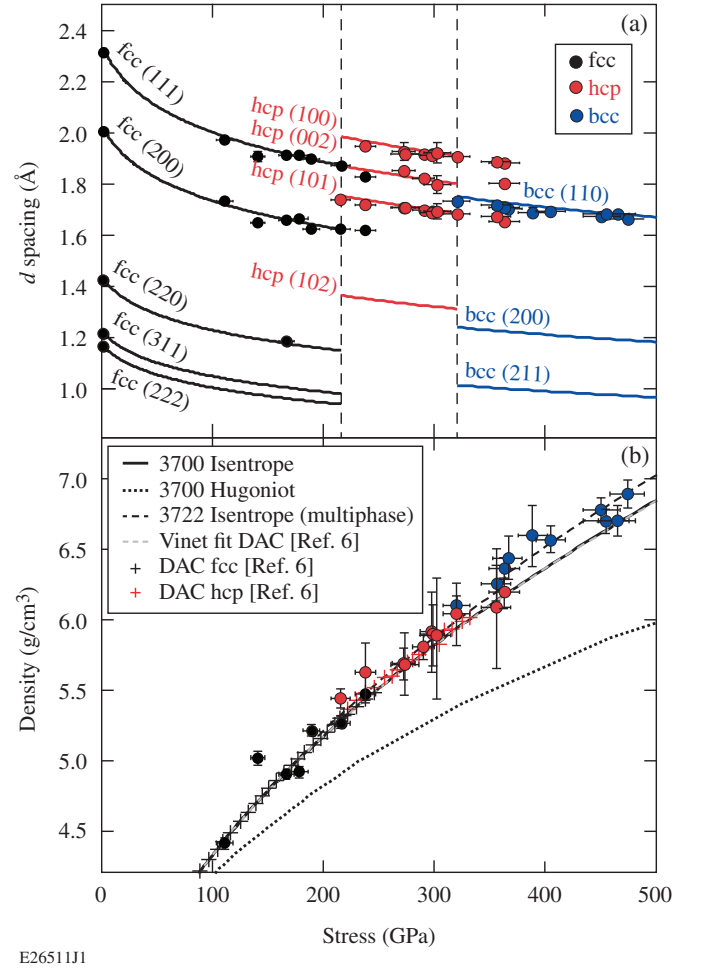

FIG. 3: (a) A comparison of the measured d-spacing versus stress from this work (solid circles), the 3700 Al principal isentrope (continuous lines). The two vertical lines are drawn at the measured transition pressures onset for the fcc–hcp and hcp–bcc transformations. (b) The corresponding density versus stress plot of the same data as (a) compared to the 3700 principal isentrope (solid), 3700 principal Hugoniot (dotted), multiphase 3722 principal isentrope (dashed), DAC fcc data (black cross), DAC hcp data (red cross), and Vinet EOS fit to the DAC data (gray dash)[10].

for the fcc–hcp and hcp–bcc transitions. The fcc–hcp coexistence has been observed in other materials, including Xe [25], due to the development of stacking disorder in the fcc lattice to form hcp.

Figure 3(b) is a plot of Al density, determined from a fit to the observed structures versus the stress. The weighted average of the measured c/a ratios for the hcp phase is 1.65±0.01 and is independent of pressure. The measurements are compared to the free-energy–based Kerley 3700 EOS [26], the DFT based *SESAME* 3722 multiphase EOS [15], and DAC data[10]. The data best agree with the *SESAME* 3722 table that includes changes in volume across the phase boundaries, that were measured to be approximately 3.2±0.3% and 2.7±0.6% for

the fcc–hcp and hcp–bcc transitions, respectively. The *SESAME* 3722 calculated transition pressures are 10% lower and 13% higher than the measured pressure onsets for the fcc–hcp and hcp–bcc transitions, respectively.

We observe a significant change in the texture of the Al when undergoing a transition from hcp to the bcc structure. In Fig. 2(a), the strong initial texture of the Al foil is evident in the (111) fcc Al line because of its limited extent compared to the calibration lines from the uncompressed polycrystalline W pinhole. The initial texture of the rolled foil Al samples was characterized using Philips X'Pert Resolution Materials Research Diffractometer. The pole figures and data show the $(200)_{fcc}$ plane normals are nearly parallel ($\smile 0°$ to $15°$) to the pressure-loading axis, and the $(111)_{fcc}$ plane normals have a preferred orientation of $\smile 40°$ to $60°$ with respect to the pressure-loading direction. A strong texture persists through the fcc–hcp Al transition as seen in the hcp lines [Figs. 2(b) and 2(c)]. A comparison of fcc and hcp diffraction patterns shows that the azimuthal dependence of the Debye–Scherrer ring intensity of the $(111)_{fcc}$ line and the $(002)_{hcp}$ line is nearly the same through the fcc→hcp transition. This strong correlation suggests parallelism of the close-packed planes is maintained through the transformation and satisfies one requirement for the Shoji–Nishiyama orientation relationship (OR) [27]. In contrast, the Debye–Scherrer rings for bcc Al [Fig.2(d)], exhibiting greater azimuthal extent, indicate more randomly oriented grains, as expected for a rearrangement from a close-packed to non-close-packed structure. However, the strong features in the texture of the $(111)_{fcc}$ and $(002)_{hcp}$ lines are still seen, less dramatically, in the $(110)_{bcc}$ line. The new bcc texture indicates the fairly close-packed $\{110\}_{bcc}$ planes are parallel to the close-packed $\{002\}_{hcp}$ planes, consistent with the Burgers OR [28]. These texture data suggest Al is an excellent candidate for future studies that will investigate the atomic pathways through diffusionless phase transformations.

In summary, these results extend Al XRD data to 475 GPa. The hcp to bcc phase transition in highly compressed Al was observed to occur at a pressure of 321 ± 12 GPa. In addition, the fcc to hcp phase transition was observed to occur at a pressure of 216 ± 9 GPa under nanosecond ramp-compression conditions. The stress-density data are in better agreement with the DFT-based *SESAME* 3722 isentrope than the previously calculated Kerley 3700 isentrope. In addition, the texture evolution shows that on nanosecond timescales, atoms rearrange in spaces between close packed planes.

* Electronic address: dpol@lle.rochester.edu

[1] J. C. Boettger and S. B. Trickey, Phys. Rev. B **53**, 3007 (1996).

[2] G. V. Sin'ko and N. A. Smirnov, J. Phys.: Condens. Matter **14**, 6989 (2002).

[3] V. Mishra and S. Chaturvedi, Physica B **393**, 278 (2007).

[4] M. J. Tambe, N. Bonini, and N. Marzari, Phys. Rev. B **77**, 172102 (2008).

[5] A. C. Mitchell and W. J. Nellis, J. Appl. Phys. **52**, 3363 (1981).

[6] W. J. Nellis, J. A. Moriarty, A. C. Mitchell, M. Ross, R. G. Dandrea, N. W. Ashcroft, N. C. Holmes, and G. R. Gathers, Phys. Rev. Lett. **60**, 1414 (1988).

[7] C. E. Ragan III, Phys. Rev. A **25**, 3360 (1982).

[8] P. M. Celliers, G. W. Collins, D. G. Hicks, and J. H. Eggert, J. Appl. Phys. **98**, 113529 (2005).

[9] M. D. Knudson, M. P. Desjarlais, and A. Pribram-Jones, Phys. Rev. B **91**, 224105 (2015).

[10] Y. Akahama, M. Nishimura, K. Kinoshita, H. Kawamura, and Y. Ohishi, Phys. Rev. Lett. **96**, 045505 (2006).

[11] C. J. Pickard and R. J. Needs, Nat. Mater. **9**, 624 (2010).

[12] J.-P. Davis, J. Appl. Phys. **99**, 103512 (2006).

[13] R. F. Smith, J. H. Eggert, A. Jankowski, P. M. Celliers, M. J. Edwards, Y. M. Gupta, J. R. Asay, and G. W. Collins, Phys. Rev. Lett. **98**, 065701 (2007).

[14] R. W. Lemke, D. H. Dolan, D. G. Dalton, J. L. Brown, K. Tomlinson, G. R. Robertson, M. D. Knud-

son, E. Harding, A. E. Mattsson, J. H. Carpenter, *et al.*, J. Appl. Phys. **119**, 015904 (2016).

[15] T. Sjostrom, S. Crockett, and S. Rudin, Phys. Rev. B **94**, 144101 (2016).

[16] J. A. Moriarty, D. A. Young, and M. Ross, Phys. Rev. B **30**, 578 (1984).

[17] R. Boehler and M. Ross, Earth and Planet. Sci. Lett. **153**, 223 (1997).

[18] A. Vailionis, E. G. Gamaly, V. Mizeikis, W. Yang, A. V. Rode, and S. Juodkazis, Nat. Commun. **2**, 445 (2011).

[19] D. D. Meyerhofer, J. Bromage, C. Dorrer, J. H. Kelly, B. E. Kruschwitz, S. J. Loucks, R. L. McCrory, S. F. B. Morse, J. F. Myatt, P. M. Nilson, *et al.*, in *J.Phys.: Conf. Ser.*, Vol. 244, p. 032010.

[20] J. R. Rygg, J. H. Eggert, A. E. Lazicki, F. Coppari, J. A. Hawreliak, D. G. Hicks, R. F. Smith, C. M. Sorce, T. M. Uphaus, B. Yaakobi, *et al.*, Rev. Sci. Instrum. **83**, 113904 (2012).

[21] P. M. Celliers, D. K. Bradley, G. W. Collins, D. G. Hicks,

T. R. Boehly, and W. J. Armstrong, Rev. Sci. Instrum. **75**, 4916 (2004).

[22] P. A. Rigg, M. D. Knudson, R. J. Scharff, and R. S. Hixson, J. Appl. Phys. **116**, 033515 (2014).

[23] D. E. Fratanduono, T. R. Boehly, M. A. Barrios, D. D. Meyerhofer, J. H. Eggert, R. F. Smith, D. G. Hicks, P. M. Celliers, D. G. Braun, and G. W. Collins, J. Appl. Phys. **109**, 123521 (2011).

[24] Y. B. Kudasov, O. M. Surdin, A. S. Korshunov, V. N. Pavlov, N. V. Frolova, and R. S. Kuzin, J. Exp. Theor. Phys. **117**, 664 (2013).

[25] H. Cynn, C. S. Yoo, B. Baer, V. Iota-Herbei, A. K. McMahan, M. Nicol, and S. Carlson, Phys. Rev. Lett. **86**, 4552 (2001).

[26] G. I. Kerley, Int. J. Impact Eng. **5**, 441 (1987).

[27] Z. Nishiyama, *Martensitic transformation*, 1st ed., Materials Science Series (Academic Press, New York, 1978).

[28] W. G. Burgers, Physica **1**, 561 (1934).